Inorganic Chemistry

ARTICLE

pubs.acs.org/IC

Synthesis, Characterization, and Electrochemical Properties of a Series of Sterically Varied Iron(II) Alkoxide Precursors and Their Resultant Nanoparticles

Timothy J. Boyle,* Leigh Anna M. Ottley, Christopher A. Apblett, Constantine A. Stewart, Sarah M. Hoppe, Krista L. Hawthorne, and Mark A. Rodriguez

Sandia National Laboratories, Advanced Materials Laboratory, 1001 University Boulevard, Southeast, Albuquerque, New Mexico 87106, United States

Supporting Information

ABSTRACT: A new family of iron(II) aryloxide $[Fe(OAr)_2(py)_x]$ precursors was synthesized from the alcoholysis of iron(II) mesityl $[Fe(Mes)_2]$ in pyridine (py) using a series of sterically varied 2-alkyl phenols (alkyl = methyl (H-*o*MP), isopropyl (H-*o*PP), *tert*-butyl (H-*o*BP)) and 2,6-dialkyl phenols (alkyl = methyl (H-DMP), isopropyl (H-DIP), *tert*-butyl (H-DBP), phenyl (H-DPhP)). All of the products were found to be mononuclear and structurally characterized as $[Fe(OAr)_2(py)_x]$ (x = 3 OAr = *o*MP (**1**), *o*PP (**2**), *o*BP (**3**), DMP (**4**), DIP (**5**); x = 2 OAr = DBP (**6**), DPhP (**7**)). The use of tris-*tert*-butoxysilanol ($OSi(OBu^t)_3$ = TOBS) led to isolation of $[Fe(TOBS)_2(py)_2]$ (**8**). The new $Fe(OAr)_2(py)_x$ (**1**−**6**) were found, under solvothermal conditions, to produce nanodots identified by PXRD as the γ-maghemite phase. The model precursor **3** and the nanoparticles **6n** were evaluated using electrochemical methods. Cyclic voltammetry for **3** revealed multiple irreversible oxidation peaks, which have been tentatively attributed to the loss of alkoxide ligand coupled with the deposition of a solid Fe-containing coating on the electrode. This coating was stable out to the voltage limits for the acetonitrile solvent.

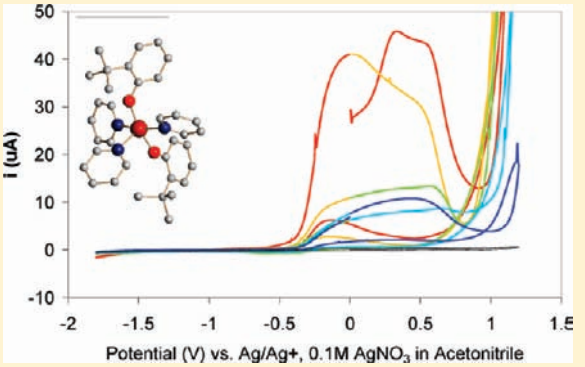

INTRODUCTION

The literature on structurally characterized, complex iron alkoxides $[Fe(OR)_x]$ is voluminous with over 2000 species reported that contain at least one Fe and two OR groups.[1] However, from this large family of compounds, surprisingly few are the simple $[Fe(OR)_x]$ (x = 2 or 3) species.[2−9] These simple $[Fe(OR)_x]$ molecules are important for a diverse number of applications ranging from biological processes to power storage to magnetic devices to fundamental research appeal. Our interest in these compounds lies in the utility of iron-based materials for lithium-ion batteries due to their low cost, low hazard concerns, 'green' nature of the material, and potential for high theoretical energy density. Of these, bulk iron oxide (FeO_x) and lithium iron oxide ($LiFeO_x$) materials have been previously explored as potential lithium-ion battery materials but were quickly abandoned due to their poor performance.[10−14]

The olivine structure of lithium iron phosphate $[LiFe(PO_4)]$ along with the delithiated phase of iron phosphate $[Fe(PO_4)]$ have garnered recent interest not only for their 'green' properties but also for their reported high power, high specific capacity, high natural abundance, high specific energy, long cycle life, stable structure, low toxicity, low pollution, and low cost.[15−26] As these materials in the bulk phase were explored some issues arose that could limit their utility, such as poor electronic conductivity and low lithium-ion diffusion coefficient. Recent results indicate that production of nanoscaled $[Fe(PO_4)]$[19−21] and $[LiFe(PO_4)]$[19,20,22−26] may overcome these disadvantages. It was reasoned that if the Fe-based phosphates were improved by moving to the nanoregime, the Fe-based oxides may also benefit from a similar reduction in size. It has been reported in several studies where the nanoparticles of FeO_x (200−250 mAh/g, 425−500 mWh/g)[14,27−29] and $Li_zFe_yO_x$ (140−150 mAh/g)[30,31] demonstrated high capacities.[13,32−37] Therefore, we were interested in exploring the electrochemical behavior of FeO_x nanoparticles. A wide number of commercially available and designer precursors have been used to generate a variety of morphologically varied FeO_x-based nanomaterials.

Interestingly, the use of iron alkoxide ($[Fe(OR)_n]$, where n = 2 or 3) precursors for production of FeO_x nanomaterials has been surprisingly understudied.[38−48] These compounds were of interest since we previously demonstrated that the structure of the metal alkoxide $[M(OR)_x]$ precursor plays a vital role in controlling the properties (i.e., morphology, phase, size, etc.) of the final nanomaterials.[49−51] Therefore, we undertook the synthesis and characterization of a series of sterically varied $[Fe(OR)_x]$

Received: March 1, 2011
Published: June 03, 2011

focusing on aryloxide (OAr) ligands. Several synthetic approaches were explored with the alkyl−alcohol exchange ultimately becoming the preferred route due to a higher yield and purer crude products. For this study, iron(II) mesityl ([$Fe(Mes)_2$]; Mes = $C_6H_2(CH_3)_3$-2,4,6) was reacted with a series of 2-alkyl phenols (alkyl = methyl (H-*o*MP), isopropyl (H-*o*PP), *tert*-butyl (H-*o*BP)) and 2,6-dialkyl phenols (alkyl = methyl (H-DMP), isopropyl (H-DIP), *tert*-butyl (H-DBP), phenyl (H-DPhP)) as shown in eq 1. The products were crystallographically characterized exclusively as monomers: [$Fe(OAr)_2(py)_3$], where OAr = *o*MP (**1**), *o*PP (**2**), *o*BP (**3**), DMP (**4**), DIP (**5**), [$Fe(OAr)_2(py)_2$], where OAr = DBP (**6**), DPhP (**7**), and [$Fe(TOBS)_2(py)_2$] (**8**), where TOBS = $OSi(OCMe_3)_3$. Once isolated, compounds **1**−**6** were used to generate nanoparticles following a solvothermal (SOLVO) process. The model precursor **3** and the **6n** nanoparticles were preliminarily studied using electrochemical methods to establish their baseline properties for lithium-ion battery applications

$$[Fe(Mes)_2] + 2H{-}OAr \xrightarrow{py} [Fe(OAr)_2(py)_x] + 2H{-}Mes \quad (1)$$

n = 3: OAr = *o*MP (**1**), *o*PP (**2**), *o*BP (**3**), DMP (**4**), DIP (**5**). n = 2: OAr = DBP (**6**), DPhP (**7**), TOBS (**8**).

EXPERIMENTAL SECTION

All compounds and reactions described were handled with rigorous exclusion of air and water using standard Schlenk line and argon-filled glovebox techniques. All solvents were stored under argon and used as received in (Aldrich) Sure/Seal bottles, including toluene (tol) and pyridine (py). The following chemicals were used as received (Aldrich and Alfa Aesar): [BrMg(Mes)] (1.0 M in THF), $FeBr_2$, H-*o*MP, H-*o*PP, H-*o*BP, H-DMP, H-DIP, H-DBP, H-DPhP, and H-TOBS. [$Fe(Mes)_2$] was synthesized from the reaction of $FeBr_2$ in THF/2,4-dioxane (5:1) with 2 equiv of [BrMg(Mes)].[52,53] FTIR data were obtained for KBr pressed pellets using a Bruker Vector 22 Instrument under an atmosphere of flowing nitrogen. Elemental analyses were performed on a Perkin-Elmer 2400 CHN-S/O Elemental Analyzer. Gas chromotography-mass spectrum (GC-MS) data were obtained on a Hewlett-Packard model 5890/5972A Series with a HP-1 cross-linked methylsilicone gum column 60 m × 0.25 mm (0.25 μm film thickness) (HP part no. 19091Z-436). Typical run conditions were as follows: (i) preheated oven at 50 °C with a ramp rate of 4.0 °C/min to a final temperature of 200 °C and held for 2.0 min. The mass spectrometer conditions for evaluation were (i) solvents from 10 to 450 atomic mass units (amu) to detect for water and (ii) all other samples from 45 to 450 amu.

General Synthesis. In an argon-filled glovebox, the appropriate H−OAr previously dissolved in pyridine was added to a vial of $Fe(Mes)_2$ in pyridine. After stirring for 12 h, the volume of the reaction mixture was drastically reduced by vacuum distillation. The resulting mixtures were set aside with their caps loose until crystals formed. The crystals that were isolated were used for all subsequent analyses. Yields were not optimized.

*[Fe(oMP)$_2$(py)$_3$] (**1**).* Used $Fe(Mes)_2$ (0.500 g, 1.71 mmol), H-*o*MP (0.370 g, 3.42 mmol), and ∼10 mL of py. Yield 75.4% (0.655 g). FTIR (KBr pellet, cm^{-1}): 3054(m), 3006(m), 2829(m), 1591(s), 1571 (m,sh), 1482(s), 1444(s), 1295(s), 1262(s), 1212(s), 1150(m), 1112(m), 1069(m), 1034(m), 1004(m), 950(w), 918(w), 866(m), 803(w), 753(s), 715(s), 698(s), 663(m), 619(m), 598(m), 459(br,m). Anal. Calcd for $C_{29}H_{29}FeN_3O_2$ (MW = 507.42): C, 68.65; H, 5.76; N, 8.28. Found: C, 68.21; H, 5.88; N, 7.86.

*[Fe(oPP)$_2$(py)$_3$] (**2**).* Used $Fe(Mes)_2$ (0.500 g, 1.71 mmol), H-*o*PP (0.466 g, 3.42 mmol), and ∼5 mL of py. Yield 62.2% (0.600 g). FTIR (KBr pellet, cm^{-1}): 3059(br, w), 2960(s), 2866(w), 1603(m), 1590(m), 1480(s), 1444(s), 1382(w), 1342(w), 1359(w), 1289(m), 1261(m), 1190(w), 1150(w), 1082(m), 1069(m), 1034(m), 931(w), 895(w), 853(m), 827(w), 803(w), 752(s), 700(s), 619(br, m), 484(br, m). Anal. Calcd for $C_{33}H_{37}FeN_3O_2$ (MW = 563.51): C, 70.33; H, 6.62; N, 7.46. Found: C, 69.88; H, 6.51; N, 7.54.

*[Fe(oBP)$_2$(py)$_3$] (**3**).* Used $Fe(Mes)_2$ (0.500 g, 1.71 mmol), H-*o*BP (0.514 g, 3.42 mmol), and ∼5 mL of py. Yield 34.7% (0.350 g). FTIR (KBr pellet, cm^{-1}): 3069(br, w), 2996(s), 2950(m), 2905(w), 2866 (w), 1596(m), 1522(m), 1477(s), 1435(s), 1383(s), 1348(s), 1306(s), 1286(w), 1263(w), 1235(w), 1213(s), 1151(s), 1121(s), 1085(s), 1068(s), 1058(s), 1045(s), 1035(s), 1005(s), 926(m), 871(s), 842(s), 823(s), 756(s), 739(s), 699(s), 652(s), 632(m), 620(s), 599(s), 571(w), 505(s), 444(s), 422(s). Anal. Calcd for $C_{35}H_{41}FeN_3O_2$ (MW = 591.56): C, 71.06; H, 6.99; N, 7.10; for $C_{30}H_{36}FeN_2O_2$ (MW = 512.46, equivalent to −1 py): C, 70.31; H, 7.08; N, 5.47. Found: C, 69.52; H, 5.54; N, 6.11.

*[Fe(DMP)$_2$(py)$_3$] (**4**).* Used $Fe(Mes)_2$ (0.500 g, 1.71 mmol), H-DMP (0.418 g, 3.42 mmol), and ∼5 mL of py. Yield 43.6% (0.40 g). FTIR (KBr pellet, cm^{-1}): 2944(s), 2924(s), 1589(m), 1467(s), 1445(s), 1422(s), 1292(m), 1263(m), 1236(w), 1213(m), 1087(s), 1070(s), 1040(s), 861(m), 803(m), 759(s), 701(s), 663(w), 540(m), 468(br, m). Anal. Calcd for $C_{31}H_{33}FeN_3O_2$ (MW = 535.45): C, 69.54; H, 6.21; N, 7.85. Found: C, 64.00; H, 6.16; N, 5.11.

*[Fe(DIP)$_2$(py)$_3$] (**5**).* Used $Fe(Mes)_2$ (0.500 g, 1.71 mmol), H-DIP (0.611 g, 3.42 mmol), and ∼5 mL of py. Yield 64.0% (0.710 g). FTIR (KBr pellet, cm^{-1}): 3055(m), 3003(w), 2960(s), 2945(sh), 2866(m), 1690(m), 1599(m), 1431(s), 1380(w), 1358(sh), 1338(m), 1262(s), 1211(m), 1130(w), 1097(m), 1067(m), 1039s), 890(m), 857(m), 803(m), 750(s), 700(s), 469(br, m). Anal. Calcd for $C_{39}H_{49}FeN_3O_2$ (MW = 647.66): C, 72.32; H, 7.63; N, 6.49. Found: C, 71.59; H, 7.63; N, 6.46.

*[Fe(DBP)$_2$(py)$_2$] (**6**).* Used $Fe(Mes)_2$ (0.500 g, 1.71 mmol), H-DBP (0.706 g, 3.42 mmol), and ∼5 mL of py. Yield 46.7% (0.510 g). FTIR (KBr pellet, cm^{-1}): 2956(s), 2916(sh), 2874(sh), 1601(m), 1509(w), 1443(s), 1405(s), 1381(m), 1358(sh, m), 1282(m), 1262(s), 1232(m), 1216(m), 1151(m), 1094(s), 1069(m), 1040(m), 1025(m), 873(m), 797(m), 748(s), 704(s), 661(m), 499(m) 459(br, m). Anal. Calcd for $C_{38}H_{52}FeN_2O_2$ (MW = 624.67): C, 73.06; H, 8.39; N, 4.48. Found: C, 72.93; H, 7.85; N, 5.73.

*[Fe(DPhP)$_2$(py)$_2$] (**7**).* Used $Fe(Mes)_2$ (1.00 g, 3.40 mmol), H-DPhP (1.68 g, 6.81 mmol), and ∼10 mL of py. Yield 72.1% (1.73 g). FTIR (KBr pellet, cm^{-1}): 3519(s), 3103(m), 3058(s), 3036(m), 3022 (m), 2959(m), 2923(s), 2588(s), 1638(s), 1599(s), 1580(m), 1561 (w), 1493(w), 1483(w) 1458(sh), 1454(s), 1445(s), 1412(s), 1364(w), 1328(w), 1311(m), 1293(s), 1272(m), 1255(m), 1223(m), 1214(w), 1172(w), 1157(w), 1103(w), 1084(w), 1069(m), 1038(m), 1028(m), 1010(m), 997(w), 915(w), 862(s), 852(w), 802(m), 756 (s), 749(s), 700(s), 627(m), 608(m), 598(m), 588(m), 515(w), 482(w), 436(w), 425(m). Anal. Calcd. for $C_{46}H_{36}FeN_2O_2$ (MW = 704.62): C, 78.41; H, 5.15; N, 7.93. Found: C, 75.93; H, 5.44; N, 2.69.

*[Fe(TOBS)$_2$(py)$_2$] (**8**).* Used $Fe(Mes)_2$ (0.250 g, 0.848 mmol), H-TOBS (0.450 g, 1.70 mmol), and ∼5 mL of py. Yield 64.0% (0.403 g). FTIR (KBr pellet, cm^{-1}): 2972(s), 2927(m), 2870(w), 1560(w), 1541(w), 1508(w), 1491(w), 1450(m), 1386(m), 1362(s), 1260(m), 1241(m), 1195(s), 1087(sh), 1053(br,s), 1017(br,s), 820(s), 758(m), 703(s), 518(w), 475(w), 433(w). Anal. Calcd for $C_{34}H_{64}FeN_2O_8Si_2$ (MW = 740.90): C, 55.12; H, 8.71; N, 3.78; for $C_{63}H_{123}Fe_2N_3O_{16}Si_4$ (MW = 1401.67; equivalent of −1/2 py): C, 53.94; H, 8.84; N, 3.00. Found: C, 53.51 H, 8.73; N, 3.96.

General X-ray Crystal Structure Information.[31] Crystals were mounted onto a glass fiber from a pool of Fluorolube and immediately placed in a cold N_2 vapor stream on a Bruker AXS diffractometer

dx.doi.org/10.1021/ic200423m |*Inorg. Chem.* 2011, 50, 6174–6182

equipped with a SMART 1000 CCD detector using graphite-monochromatized Mo Kα radiation ($\lambda = 0.7107$ Å). Lattice determination and data collection were carried out using SMART Version 5.054 software. Data reduction was performed using SAINTPLUS Version 6.01 software and corrected for absorption using the SADABS program within the SAINT software package.

Structures were solved by direct methods that yielded the heavy atoms along with a number of lighter atoms or using the PATTERSON method. Subsequent Fourier syntheses yielded the remaining light-atom positions. The hydrogen atoms were fixed in positions of ideal geometry and refined using SHELXS software. The final refinement of each compound included anisotropic thermal parameters for all non-hydrogen atoms. It should be noted that crystal structures of $M(OR)_x$ often contain disorder within the atoms of the ligand chain causing higher than normal final correlations.[54−58] All final CIF files were checked at http://www.iucr.org/. Additional information concerning data collection and final structural solutions can be found in the 14 information files or by accessing CIF files through the Cambridge Crystallographic Data Base. Data collection parameters for **1**−**8** are given in Table 1.

Specific Issues. For compound **1**, a disordered py in the lattice was squeezed using PLATON. Both compounds **5** and **8** displayed disorder in the pendant carbon chains of the Pr^i and Bu^t moieties, respectively. This was modeled using standard crystallographic restraints; however; the final quality of the structure was not significantly improved, and further efforts were not pursued. Compound **6** had disorder in the coordinated py ring, and all attempts to resolve the disorder were abandoned since no improvement in the final structure was found.

Beryllium Dome X-ray Powder Patterns (BeD-XRD). Detailed information pertaining to the beryllium dome XRD (BeD-XRD) analyses has been previously disseminated.[59−61] All samples were prepared in an argon-filled glovebox using a 1 cm quartz disk (zero-background plate), where the sample was pressed into the specimen cavity, leveled, sealed, and carefully loaded into a Siemens D500 diffractometer (scan settings, 40 kV and 30 mA with a 0.04° step size, 1 s count time, range of 5−30° 2θ, 1° divergence and receiving slits; goniometer radius = 250 mm). *Note:* Only trained personnel wearing the appropriate personal protective equipment should handle the BeD equipment. If the BeD is accidentally shattered, proper safety cleanup and disposal protocols *must* be followed.

Nanoparticle Synthesis. A SOLVO route was used to generate nanomaterials from dissolution of the desired crystalline material in py (0.50 g/20 mL) under an atmosphere of argon. This solution was then sealed in a Teflon-lined Parr acid digestion bomb and then heated to 200 °C for 24 h. After cooling to room temperature each reaction bomb was opened in air, the reaction mixture transferred to centrifuge tubes and centrifuged, and the supernatant decanted from the precipitate. The precipitate was then washed three times with hexanes, and the resulting powder was allowed to dry at room temperature under ambient conditions.

For transmission electron microscopy (TEM) analyses, the desired powder was slurried in MeOH and then a small aliquot was placed directly onto a holey-carbon copper-coated TEM grid (200 mesh from Electron Microscopy Sciences) and allowed to dry in air. The resultant particles were studied using a Philips CM 30 TEM operating at 300 kV accelerating voltage. In addition, the powder was characterized using powder XRD on a PANalytical X'Pert Pro using Cu Kα radiation with a step size of 0.0167°, with a 0.152°/s dwelling time. Dried crystalline powders were mounted directly onto a zero background holder.

Electrochemical Analysis. All cyclic voltammetry (CV) analyses were performed using a PAR2273 in potentiostatic mode at room temperature using a sweep rate of 25 mV/s. The sweep ran from the reference potential following an anodic sweep with the following setup: (i) $Ag/AgNO_3$ (0.1 M in CH_3CN) reference electrode with a ceramic frit (BASi), (ii) a 1 M $Bu_4N^+PF_6^-$ in CH_3CN sample blank solution, (iii) a polished (0.05 μm alumina paste (Beuhler)) 3 mm platinum working electrode, and (iv) a Pt wire (BASi) counter electrode. All sample solutions were prepared, and all cyclic voltammagrams (CV) were collected under an argon atmosphere. For **3**, initially CV scans were collected on a blank solution for 5 cycles to obtain a meaningful background.

Electrode preparation for cyclic voltammetry measurements in water was undertaken using a solution of 5 wt % sulfonated fluorine-substituted polyethylene or Nafion (Sigma-Aldrich) dissolved in a mixture of low-weight aliphatic alcohols. To this solvent mixture graphite (Timrex KS6, Timcal Corp.) was added to generate a solids ratio of 25:75 wt % polymer:graphite followed by stirring (10 min at room temperature) until a low-viscosity mixture formed. Approximately 100 μL of this slurry was subsequently drop cast onto a glassy carbon electrode (Bioanalytical Systems). To prepare the nanoparticle electrode, a similar preparation was synthesized and processed as noted above with inclusion of 0.2 g of **6n** in the slurry. Electrochemical measurements in water were performed using a Bioanalytical Systems Epsilon potentiometer at 25 mV/s at room temperature. A saturated Ag/AgCl electrode was used as a reference, Pt as the counter electrode, and 1 M H_2SO_4 in DI water as the electrolyte. Solutions were measured in both aerated and deaerated (nitrogen purge for 12 h) conditions.

RESULTS AND DISCUSSION

Prior to initiating a study on the electrochemical behavior of FeO_x nanoparticles, the use of $[Fe(OR)_x]$ precursors with well-understood structural properties was desired. This is due to the fact that the size, shape, and composition of the final nanomaterials have been shown to be directly impacted by the structure of the $[M(OR)_x]$ precursor.[49−51] Unfortunately, there is a surprisingly small number of structures reported for this family of compounds including the following: (i) the oxo derivatives $[Fe_9(\mu_3\text{-}O)_3(\mu\text{-}OEt)_5(OEt)_6(HOEt)]$[9] ($OCH_2CH_3$ (OEt)) and $[Fe_5(\mu_5\text{-}O)(\mu\text{-}OR)_8(OR)_5]$ (where OR = OEt,[5,6] $OCH(CH_3)_2$ (OPr^i)[3]); (ii) the alkoxides $[Fe(OPr^i)_3]$[8] and $[Fe(\mu\text{-}OR)(OR)_2]_2$ [where OR = {$OC(CH_3)_2R$: R = CH_3,[4,7] CH_2CH_3[3]}, $OC(CH_3)_2(C_6H_5)$,[5] $OCH(C_6H_5)_2$[48]], $[Fe(OCPh_3)(THF)_2]$,[2] and (iii) the aryloxides $[Fe(\mu\text{-DBP-}Bu^t\text{-}4)(DBP\text{-}Bu^t\text{-}4)]_2$,[2] $[Fe(OC_6H_3\text{-}[C_6H_3(CH(CH_3)_2)_2\text{-}2,6]\text{-}2,6]$,[46] $[(OR)^cFe(\mu^c\text{-}OR)]_2$ (OR = $OC_6H_4(CH_2N(CH_3)_2)$-2; c = chelating] and $[(py)_2Fe(OC_6H_3\text{-}(CH_2N(CH_3)_2)_2{}^c\text{-}2,6]$.[47] One reason for this crystallographic lacuna may be due to the reported insolubility of Fe(II) alkoxides.[62] Therefore, it became necessary to synthesize highly soluble $[Fe(OR)_x]$ nanoparticle precursors which could be crystallographically characterized. From the wide array of alkoxide ligands available, based on previous experience, the ortho-substituted phenols were ideal ligands for this study due to their commercial availability, variations in steric bulk of the phenol, and known value in reducing oligomerization.[54−58,63−67]

Several synthetic routes to the $[Fe(OAr)_x]$ of interest were explored. Initially, the aminolysis (eqs 2a and 2b in THF) route was used for both Fe(II) and Fe(III) metal centers. From eq 2a, the following crystals were of high enough quality to yield a structure solution (see Table 1): $[Fe(DBP)_2(THF)(py)]$ (**1S**), $[Fe(DPhP)_3]$ (**2S**), or $[Fe(DPhP)_2(THF)_2]$ (**3S**); figures are available in the Supporting Information. Unfortunately, these and other products isolated were (i) contaminated (with alkali metal and/or halides), attributed to the difficulty in preparing pure $Fe(NR_2)_n$, (ii) variable in final oxidation states, and/or (iii) insoluble. Due to these inconsistent results, these routes (eqs 2a and 2b) were abandoned.

dx.doi.org/10.1021/ic200423m |*Inorg. Chem.* 2011, 50, 6174–6182

Table 1. Data Collection Parameters for 1−8 and 1S−3S

compound	1[c]	2	3	4
chemical formula	$C_{29}H_{29}Fe\ N_3O_2$	$C_{33}H_{37}FeN_3O_2$	$C_{35}H_{41}FeN_3O_2$	$C_{31}H_{33}FeN_3O_2$
fw	507.40	563.51	591.56	535.45
temp (K)	173(2)	173(2)	173(2)	173(2)
space group	orthorhombic, *Fddd*	monoclinic, *C*2/*c*	monoclinic, *C*2/*c*	monoclinic, *C*2/*c*
a (Å)	13.493(2)	34.823(4)	37.654(6)	13.5680(19)
b (Å)	28.102(5)	16.292(2)	13.255(2)	11.6850(16)
c (Å)	29.703(5)	17.320(2)	25.791(4)	19.236(3)
β (deg)		110.544(3)	128.674(5)	104.329(2)
V (Å^3)	11263(3)	9201(2)	10049(3)	2954.8(7)
Z	16	12	12	4
D_{calcd}(Mg/m^3)	1.197	1.220	1.173	1.204
μ (Mo, Kα) (mm^{-1})	0.563	0.524	0.483	0.540
R1[a] (%) (all data)	5.87(6.90)	5.49(8.44)	3.62(4.93)	3.16(3.67)
wR2[b] (%) (all data)	12.37(12.90)	12.14(14.83)	8.24(8.92)	7.74(8.05)

compound	5	6	7	8
chemical formula	$C_{39}H_{49}FeN_3O_2$	$C_{38}H_{52}FeN_2O_2$	$C_{46}H_{36}FeN_2O_2$	$C_{34}H_{64}FeN_2O_8Si_2$
fw	647.66	624.67	704.62	740.90
temp (K)	173(2)	173(2)	173(2)	173(2)
space group	orthorhombic, *Pbca*	monoclinic, *P*2(1)/*c*	monoclinic, *P*2(1)/*n*	tetragonal, *P*4(3)2(1)2
a (Å)	14.461(3)	21.884(3)	13.131(2)	10.7648(6)
b (Å)	18.341(3)	16.018(2)	15.622(3)	10.7648(6)
c (Å)	27.896(5)	20.621(3)	19.182(4)	37.937(3)
β (deg)		104.327(2)	109.558(3)	
V (Å^3)	7399(2)	7003.4(15)	3707.9(12)	4396.2(5)
Z	8	8	4	4
D_{calcd}(Mg/m^3)	1.163	1.185	1.262	1.119
μ,(Mo, Kα) (mm^{-1})	0.443	0.464	0.447	0.440
R1[a] (%) (all data)	6.38(13.47)	5.59(6.78)	2.73(2.92)	4.63(5.33)
wR2[b] (%) (all data)	12.07(14.77)	12.16(12.97)	7.37(7.53)	11.19(11.74)

compound	1S	2S	3S
chemical formula	$C_{37}H_{55}FeNO_3$	$C_{54}\ H_{39}FeO_3$	$C_{44}H_{42}FeO_4$
fw	617.67	791.70	690.63
temp (K)	173(2)	173(2)	173(2)
space group	monoclinic, *P*2(1)/*n*	rhombohedral, *R*3	monoclinic, *C*2/*c*
a (Å)	9.740(2)	10.5954(5)	64.054(13)
b (Å)	22.662(5)	10.5954(5)	9.4340(19)
c (Å)	16.299(3)	10.5954(5)	23.507(5)
β (deg)	101.432(4)	97.2140(10)	100.035(7)
V (Å^3)	3526.2(13)	1158.57(9)	13988(5)
Z	4	1	16
D_{calcd}(Mg/m^3)	1.163	1.135	1.312
μ,(Mo, Kα) (mm^{-1})	0.461	0.365	0.475
R1[a] (%) (all data)	3.71(4.66)	7.29 (7.35)	17.18(18.39)
wR2[b] (%) (all data)	9.42(10.03)	19.05 (19.14)	28.62 (29.15)

[a] $R1 = \Sigma||F_o| - |F_c||/\Sigma|F_o| \times 100$. [b] $wR2 = [\Sigma w(F_o^2 - F_c^2)^2/\Sigma(w|F_o|^2)^2]^{1/2} \times 100$. [c] Molecule of solvent was squeezed out.

$$[Fe(N(SiMe_3)_2)_2] + 2H{-}OAr \rightarrow [Fe(OAr)_2] + 2H{-}N(SiMe_3)_2 \quad (2a)$$

$$[Fe(NMe_2)_3] + 3H{-}OAr \rightarrow [Fe(OAr)_3] + 3H{-}NMe_2 \quad (2b)$$

Since THF and the aminolysis routes proved problematic, we elected to investigate py as a solvent using the alkyl/alcoholysis exchange (eq 1). The synthesis and characterization of these $Fe(OAr)_2$ precursors, the subsequent γ-Fe_2O_3 nanoparticles, and the initial electrochemical properties of model precursors and nanoparticles are presented below.

dx.doi.org/10.1021/ic200423m |*Inorg. Chem.* 2011, 50, 6174–6182

Synthesis. Using the $[Fe(Mes)_2]$ with HOAr in pyridine proved to be a rapid, convenient, high-yield, and reproducible route to the desired family of soluble nanoparticle precursors. For each reaction the dark-red $[Fe(Mes)_2]$ powder was dissolved in pyridine and the appropriate aryl alcohol was added. The reaction mixtures darkened considerably over time with no precipitate observed after stirring for 12 h. After drastically reducing the volume of the reaction, each was set aside and allowed to slowly evaporate until crystals formed.

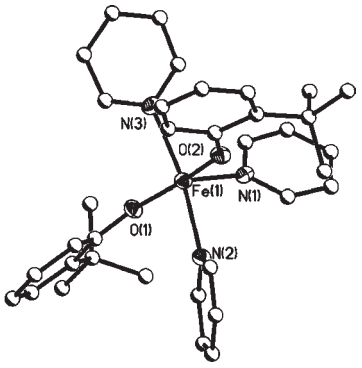

Figure 1. Structural plot of **3**. Heavy-atom thermal ellipsoids drawn at the 30% level, and carbon atoms drawn as ball and stick for simplicity. Hydrogen atoms omitted for clarity. Two molecules per unit cell.

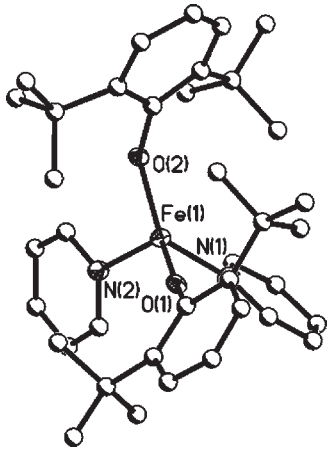

Figure 2. Structural plot of **6**. Heavy-atom thermal ellipsoids drawn at the 30% level, and carbon atoms drawn as ball and stick for simplicity. Two molecules per unit cell.

Single-Crystal Structures. As crystals of the products from eq 1 were obtained, single-crystal structures were solved to assist in determining their identity. Interestingly, for **1**−**5**, all the OAr derivatives isolated proved to be monomers with each Fe adopting a distorted square base pyramidal geometry (τ = 0.21 (**1**), 0.22 (**2**), 0.21 (**3**), 0.21 (**4**), 0.37 (**5**)).[68] A py solvent molecule occupies the apical position for each of these compounds with two trans OAr ligands and two trans py molecules in the basal positions. Compounds **6**−**8** were also found to be monomeric but adopted a distorted tetrahedral geometry. Figures 1 and 2 show the structure of representative compounds **3** and **6**, respectively. The remaining structural plots are available in the Supporting Information. The reduced number of bound solvent molecules for these compounds is presumably due to the increased steric bulk of the DBP, DPhP, or TOBS ligands. The metrical data for these $[Fe(OAr)_2(py)_x]$ are tabulated in Table 2 and were found to be consistent within this family of compounds as well as literature species.[2−9]

Bulk Powder Analyses. Analyses of the bulk powders of **1**−**8** were undertaken; however, the paramagnetic nature of the iron(II) metal center yields extremely broad NMR spectra, which makes structural interpretation difficult and verification of the purity tenuous. The majority of the compounds' elemental analyses for **1**−**8** were outside the range of the expected values and were not consistent with fully desolvated compounds. This incongruity has been previously noted for a number of solvated $M(OR)_x$ and is often attributed to preferential loss of solvent upon analysis (when possible, these are noted in in the Experimental Section) or complex thermal decomposition of the precursor.[54−58,63−67,69,70] Therefore, additional analytical methods were investigated to assist in characterizing these compounds.

For the FTIR spectra of **1**−**7**, the strong stretches above 1500 cm^{-1} (tentatively assigned as the Fe−C stretch)[71] were absent, with stretches and bends associated with the respective OAr ligands now present. Since the bonding mode around the Fe metal centers of **1**−**7** consists of Fe−O and Fe−N bonds only, the fingerprint region of the FTIR spectra of these compounds is nearly identical. Two major stretches around 750 and 700 cm^{-1} and two minor stretches located around 860 and 800 cm^{-1} were observed. The remainder of the spectrum consists of OAr and py stretches/bends. For **8**, the spectrum is greatly simplified, especially in the fingerprint region with only two major stretches at 803 and 703 cm^{-1}. There is a minor stretch at 758 cm^{-1}, and the other one may be obscured by the broad peak at 803 cm^{-1}. The changes in bond stretches must be attributed to the differences of the siloxide ligand in comparison to the aryloxides.

Table 2. Select Averaged Metrical Data for 1−8

	distance (Å)		angle (deg)		
compound	Fe-OAr/OSiR$_3$(av Å)	Fe−N$_{py}$(av Å)	O−Fe−O (av deg)	N−Fe−N (av deg)	O−Fe−N (av deg)
1	1.948(2)	2.19	157.25(15)	133.53	93.29
2	1.94	2.21	160.61(12)	134.20	92.80
3	1.94	2.30	165.68(7)	132.10	92.60
4	1.913(2)	2.21	159.23(11)	132.36	93.45
5	1.93	2.23	150.91(9)	133.59	94.24
6	1.89	2.18	132.47(9)	86.14	107.70
7	1.91	2.15	152.49(5)	95.33(5)	99.12
8	1.865(3)	2.138(3)	134.77(18)	89.35(16)	105.88

dx.doi.org/10.1021/ic200423m |*Inorg. Chem.* 2011, 50, 6174–6182

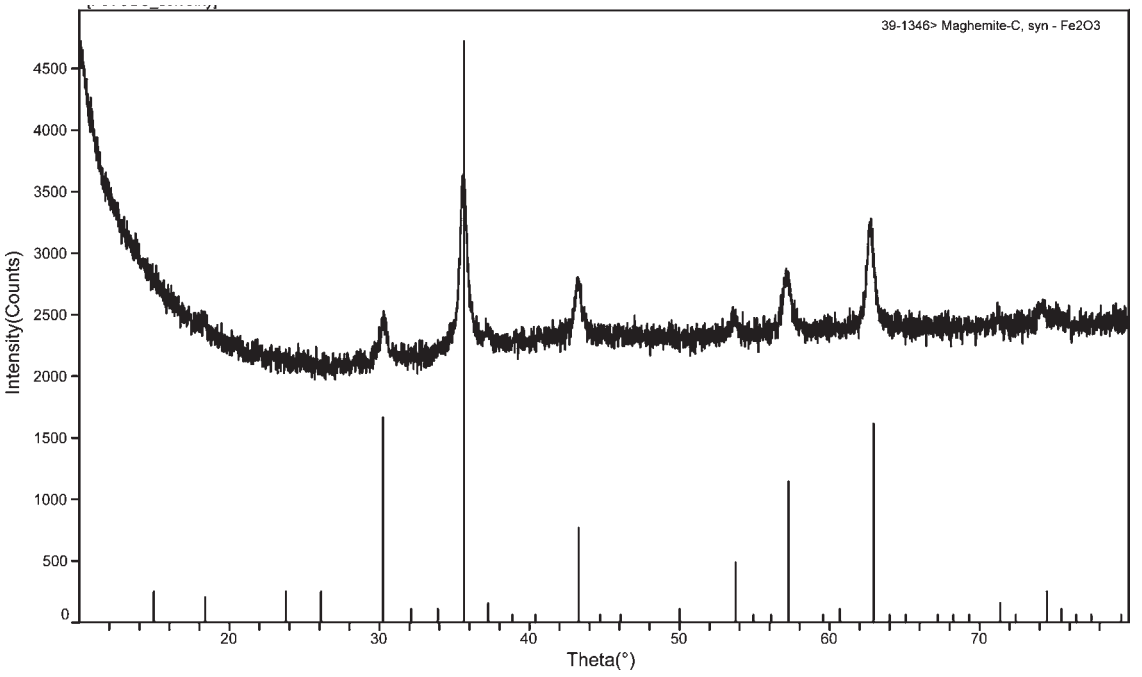

Figure 3. PXRD pattern of the representative spectrum of **8n** and library pattern for γ-maghemite (39-1348, γ-Fe_2O_3).

In general, it can be concluded that the spectra of these compounds are in agreement with each other, which implies that the bulk powders are in agreement with the single-crystal X-ray structures.

While the FTIR data is informative, it is not conclusive in terms of purity. To address this issue, we opted to focus on beryllium dome PXRD (termed BeD-XRD),[59−61] which allows for X-ray analyses of air-sensitive compounds. A comparison between the experimental data with the theoretical patterns (derived from the single-crystal structure) can lend some insight into the purity of the bulk powders. It is of note that the theoretical patterns are generated based upon an idealized random sample, whereas crystal orientation for the actual powders will favor certain *d*-spacing patterns. Further, to prepare a random sample, it is often necessary to grind the powder, which can alter the degree of solvation and affect the final powder pattern observed. Therefore, dried crystalline material that was not ground was used for each sample. The experimental patterns of the crystalline material appear to be in-line with the calculated spectra (see Supporting Information) for **3**, **4**, **6**, **7**, and **8**, whereas, the spectra of compounds **1**, **2**, and **5** are less definitive due to the texture issues noted above. Combined, the FTIR and BeD-XRD data indicate that the bulk materials are in agreement with the single-crystal structures obtained.

Nanoparticle Synthesis. With this family of well-characterized precursors in hand, it was of interest to determine their utility in producing nanomaterials of FeO_x. Using a SOLVO route, nanoparticles were successfully isolated from each precursor. For convenience, these are named based on the assigned precursor number followed by **n** (i.e., nanoparticles generated from compound **1** are named **1n**). Powder X-ray diffraction indicated that each sample produced the iron deficient γ-maghemite (PDF 39-136, γ-Fe_2O_3). Since all the XRD patterns were identical a representative PXRD pattern (**8n**) is shown in Figure 3, while the TEM images of the resultant nanomaterials for each precursor are shown in Figure 4a−i.

Since the precursors are all monomers and form the same γ-Fe_2O_3, based on the precursor structure argument, the general shape of the precursor can be used to generate preferred morphologies,[49−51] the nanoparticles should all look similar. A polydispersed set of nanodots is observed for each $[Fe(OR)_2]$ precursor. The largest and most uniform nanodots appear to be generated for **1n** (Figure 4a), **6n** (Figure 4f), **7n** (Figure 4g), and **8n** (Figure 4h), which range from 10 to 60 nm in size with the majority appearing around 40 nm in size. For **2n** (Figure 4b), **3n** (Figure 4c), and **4n** (Figure 4d), the particles observed had some similar sized nanoparticles noted for the previous compounds but the majority of particles are substantially smaller. This is especially true for **5n** (Figure 4e), where the nanoparticle appears to be uniform 12 nm sized nanoparticles. In order to determine whether the size and shape formation of the nanoparticles was a result of the thermodynamically favored species forming independent of the starting material, the $Fe(Mes)_2$ precursor was also run under similar conditions. The particles are shown in Figure 4i and appear to be more square-like in shape while maintaining the γ-Fe_2O_3 phase; however, repetition of the synthesis of these nanoparticles led to less regular square-shaped material. Therefore, the alkoxides can be attributed to favoring the formation of dots where the size variations may be attributed to slight differences in processing time and concentrations of the selected precursors. The need for more complex shaped precursors is necessary to probe this process further, and work in this area is currently underway.

Electrochemical Characterization. Little information is available concerning the electrochemical characterization of $Fe(OAr)_2$ compounds or the nanoparticles derived from them. Since the precursors were all monomeric solvated species and the nanoparticles all adopted the same phase and general morphology, only one sample from each was evaluated. Initially, a control electrolyte solution was prepared and tested to collect background voltammagrams, which found no observable reduction oxidation (redox) waves. This setup was then used to explore the

dx.doi.org/10.1021/ic200423m |*Inorg. Chem.* 2011, 50, 6174–6182

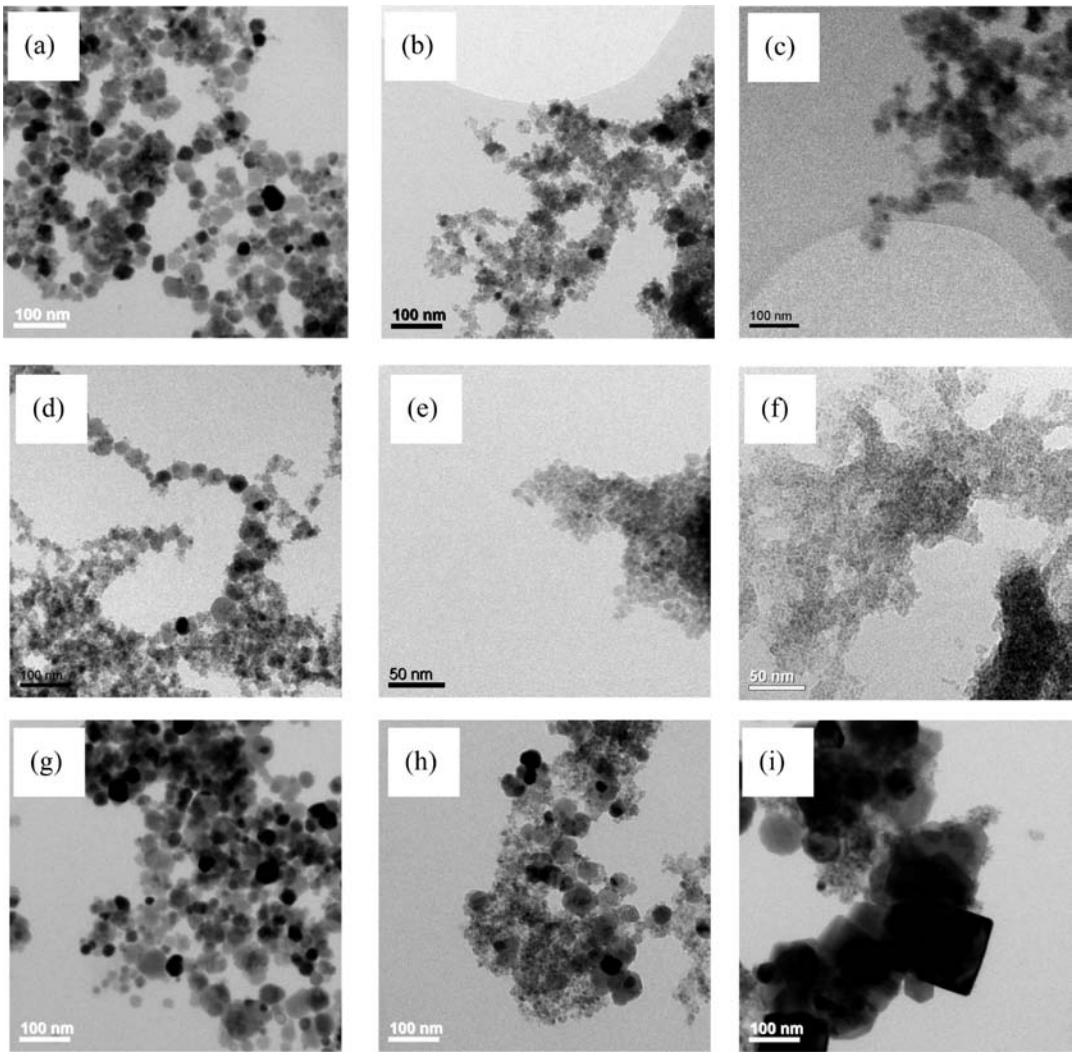

Figure 4. TEM images of (a) **1n**, (b) **2n**, (c) **3n**, (d) **4n**, (e) **5n**, (f) **6n**, (g) **7n**, (h) **8n**, and (i) nanoparticles generated from $Fe(Mes)_2$ using the SOLVO preparation route.

electrochemical results for the representative precursor (**3**) and nanoparticle (**6n**).

Compound **3** was added to an electrolyte solution of $(Bu_4N)PF_6$ in CH_3CN and scanned with the resulting cyclic voltammagram (CV) curves (oxidative to reductive) shown in Figure 5. During the initial electrochemical evaluation several oxidative peaks were observed: the final oxidative current was unresolved as a separate reaction due to the limits of the electrochemical window for the solvent chosen (acetonitrile, stability limits ~1 V to ~−2 V vs Ag/Ag^+). There were no reduction peaks present. Five cycles were run, and the intensity of these peaks decreased as the number of cycles increased. It was reasoned that as the current was applied, a coating was being deposited on the electrode and subsequent oxidation cycles yielded additional material deposition, which ultimately suppressed further oxidation of the reagents. After 5 cycles the test was stopped and the electrode visually inspected. The electrode was now a dull, brown color instead of the initial shiny metal platinum. Unfortunately, the film generated on the electrode did not yield an interpretable PXRD pattern (see Supporting Information). This can be attributed to too small of a sample to allow for meaningful data, the size of the materials formed is subnanometer in size, which significantly broadens the signal, and/or the final material being amorphous. Further analyses of the material using micro-X-ray fluorescence (XRF; see Supporting Information) indicated that Fe was present in the sample.

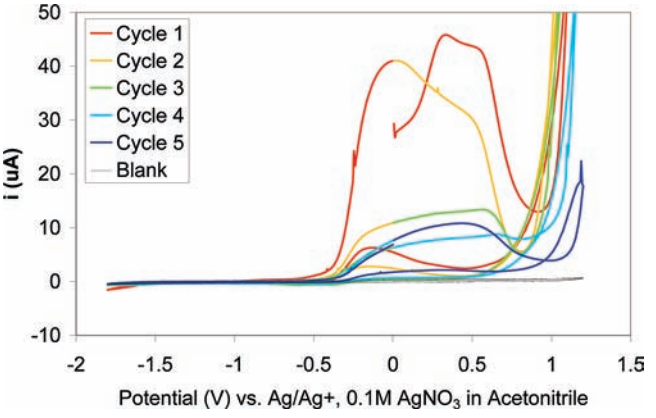

Figure 5. Cyclic voltammetry of **3** in CH_3CN.

dx.doi.org/10.1021/ic200423m |*Inorg. Chem.* 2011, 50, 6174–6182

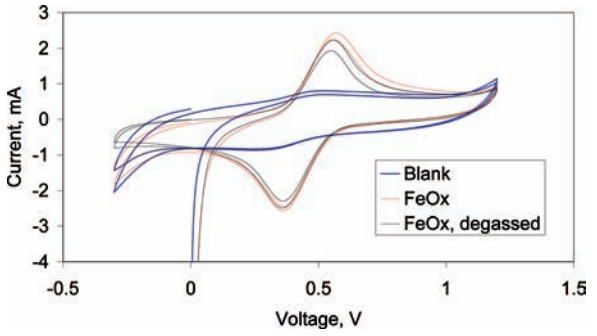

Figure 6. Porous electrode cyclic voltammetry of blank carbon porous electrode vs carbon porous electrode with **6n** added. Conditions: room temperature, 25 mV/s sweep rate, 1 M H_2SO_4 electrolyte.

Understanding the various transformations and assigning the CV peaks to specific aspects of the precursor were attempted. Initial investigations focused on determining the structural properties of **3** in CH_3CN. Recrystallization of **3** from hot CH_3CN yielded an identical crystal (**3a**). This indicates the compound is stable in hot CH_3CN and any changes that occur in the electrochemical study must be attributed to the electrochemical process only and not the solvent. The electrolyte of the cell after cycling was evaluated by GC-MS, and the full experimental data set is shown in the Supporting Information. Initially, a set of standards was run to verify retention time and the MS spectrum in the presence of the salt, yielding py at 3.87 min, CH_3CN at 5.14 min, and H-*o*BP at 25.1 min. The analysis of the resultant elute from the redox yielded three peaks at 3.87, 5.14, and 25.1 min, which were consistent with the elution time of the solvents. An initial GC-MS analysis of the **3** in CH_3CN indicates the alcohol was present as well, which may be due to the thermal break down of **3** upon injection into the GCMS. On the basis of these data and crystallization of the same structure from CH_3CN (vide infra **3a**), the first two peaks have been tentatively assigned to oxidation of the *o*BP ligand. This eventually leads to the oxide forming (vide infra PXRD) and the Fe-containing deposit found on the electrode. Additional studies are underway to fully characterize the various redox properties of these interesting precursors and explore how the ligands would effect these transformations.

As expected, a blank of polymer and graphite showed no electrochemical behavior in the voltage window explored. With the addition of **6n**, a distinct oxidation/reduction peak pair was observed (Figure 6). Deaeration of the reaction media did not significantly change the extent of oxidation and reduction observed. The midpoint potential between oxidation and reduction occurs at around 450 mV vs Ag/Ag^+, which is higher than the tabulated standard potential for iron oxidation of +240 mV vs Ag/Ag^+.[72] However, the relatively broad peaks for both oxidation and reduction peaks coupled with the porous nature of the electrode makes definitive assessment of the exact chemical potential difficult. The large separation between oxidation and reduction peaks is associated with the diffusion within the porous electrodes used in this study. What is clear from the study is that the nanoparticle iron is electroactive within the aqueous voltage window and that clear quasi-reversible oxidation and reduction is occurring. Additional work is needed to prepare nonporous electrodes that can be studied without diffusional limitations in order to better understand the oxidation and reduction of the nanoparticles themselves. In particular, the relatively large shift in standard potential observed may be due to some surface effect of the nanoparticles (and the higher energy of the surface atoms residing on the nanoparticle surface).

SUMMARY AND CONCLUSION

A novel family of $[Fe(OAr)_2(py)_x]$ precursors has been synthesized and isolated from the alcoholysis of $[Fe(Mes)_2]$ in py. On the basis of the degree of solvation, the metal centers of **1**−**5** were found to adopt a distorted square base pyramidal geometry. As more sterically demanding ligands were introduced, compounds **6**−**8** adopted a distorted tetrahedral geometry around the Fe metal center. This new family of compounds was used in a SOLVO approach to generate nanodots of γ-Fe_2O_3. Electrochemical investigation of **3** revealed that the precursor undergoes several oxidation steps that have been preliminarily assigned to the loss of OR ligand and oxidation of the Fe^{2+} metal center. Oxidation and reduction of the nanoparticles (**6n**) was observed in an aqueous electrolyte bound into a porous electrode, although potentials higher than the literature values for standard oxidation potentials were observed. More work needs to be done to see if this is due to the nano-characteristics of the material. With the baseline established to the electrochemical behavior of these nanomaterials, additional work to probe their capability to intercalate Li ions for use as lithium-ion battery cathodes is underway.

ASSOCIATED CONTENT

Supporting Information. Additional data including BeD-XRD setup and experimental BeD-XRD patterns for **1**−**8**, GC patterns of nanoparticle electrochemical solutions, GIXRD patterns of electrochemically generated materials, and structural plots of **1**−**8** and **S1**−**S3**, are available. The crystal structures of **1**−**8** and **S1**−**S3** have been deposited at the Cambridge Crystallographic Data Centre and allocated the deposition numbers CCDC 816497−816507. This material is available free of charge via the Internet at http://pubs.acs.org.

AUTHOR INFORMATION

Corresponding Author
*Phone: (505)272-7625. Fax: (505)272-7336.E-mail tjboyle@Sandia.gov

ACKNOWLEDGMENT

The authors thank Dr. S. D. Bunge, M. Trujillo, and H. D. Pratt III for technical assistance. This work was supported by the Laboratory Directed Research and Development (LDRD) program at Sandia National Laboratories. Sandia is a multiprogram laboratory operated by Sandia Corporation, a Lockheed Martin Company, for the United States Department of Energy's National Nuclear Security Administration under Contract DE-AC04-94AL85000.

REFERENCES

(1) Conquest Version 1.11, Cambridge Crystallographic Data Centre: support@ccdc.cam.ac.uk or http://www.ccdc.cam.ac.uk [CSD version 5.30 (November 2008)].

(2) Bartlett, R. A.; Ellison, J. J.; Power, P. P.; Shoner, S. C. *Inorg. Chem.* **1991**, *30*, 2888.

(3) Kusserow, M.; Spandl, J. *Z. Anorg. Allg. Chem.* **2006**, *632*, 885.

(4) Mathur, S.; Veith, M.; Sivakov, V.; Shen, H.; Huch, V.; Hartmann, U.; Gao, H.-B. *Chem. Vap. Deposition* **2002**, *8*, 277.
(5) O'Keefe, B. J.; Monnier, S. M.; Hillmyer, M. A.; Toman, W. B. *J. Am. Chem. Soc.* **2001**, *123*, 339.
(6) Seisenbaeva, G. A.; Gohil, S.; Suslova, E. V.; Rogova, T. V.; Turova, N. Y.; Kessler, V. G. *Inorg. Chim. Acta* **2005**, *358*, 3506.
(7) Spandl, J.; Kusserow, M.; Brudgam, I. *Z. Anorg. Allg. Chem.* **2003**, *629*, 968.
(8) Turova, N. Y.; Rogova, T. V.; Kozlova, N. I.; Zhirov, A. I. *Koord. Khim.* **1983**, *9*, 1244.
(9) Vieth, M.; Fratz, F.; Huch, V. *Eur. J. Inorg. Chem.* **2001**, *2001*, 367.
(10) Thackeray, M. M.; David, W. I. F.; Goodenough, J. B. *Mater. Res. Bull.* **1982**, *17*, 785.
(11) Pernet, M.; Rodriguez, J.; Gonderand, M.; Fontcuberta, J.; Strobel, P.; Joubert, J. C. *Proceedings of the ICF-5, India*, India, 1989.
(12) Bonnet, B.; Strobel, P.; Pernet, M.; Gondrand, M.; Gros, Y.; Mouget, C.; Chabre, Y. *Mater. Sci. Forum* **1992**, *91*−*93*, 345.
(13) Quintin, M.; Devos, O.; Delville, M. H.; Campet, G. *Electrochim. Acta* **2006**, *51*, 6426.
(14) Xu, J. J.; Jain, G. *Electrochem. Solid-State Lett.* **2003**, *6*, A190.
(15) Jugovic, D.; Uskokovic, D. *J. Power Sources* **2009**, *190*, 538.
(16) Chen, J. J.; Vacchio, M. J.; Chernova, N.; Zavaliji, P. Y.; Whittingham, M. S. *Solid State Ionics* **2008**, *178*, 1676.
(17) Lin, Y.; Pan, H. G.; Gao, M. X.; Miao, H.; Li, S. Q.; Wang, Y. *Surf. Rev. Lett.* **2008**, *15*, 133.
(18) Gan, L.; Park, K.; Li, J.; Benson, R. E.; Vaknin, D.; Markert, J. T.; Croft, M. C. *Condens. Matter Mater. Phys.* **2008**, *77*, 064414.
(19) Son, D.; Kim, E.; Kim, M. G.; Cho, J.; Park, B. *Appl. Phys. Lett.* **2004**, *85*, 5875.
(20) Wang, X.; Yang, X. H.; Jin, H. Y.; Zhang, Z. *J. Cryst. Growth* **2005**, *274*, 214.
(21) Hu, X. L.; Yu, J. C. *Adv. Funct. Mater.* **2008**, *18*, 880.
(22) Jaewon, L.; Xu, C.; Teja, A. S. *2004 AIChE Annual Meeting*, Austin, TX, Austin, TX, 2004; AIChE/Wiley Press: Hoboken, NJ, pp 3689−3691.
(23) Gerbaldi, C.; Meligrana, G.; Bodoardo, S.; Tuel, A.; Penazzi, N. *J. Power Sources* **2007**, *174*, 501.
(24) Caballero, A.; Cruz-Yusta, M.; Morales, J.; Santos-Pena, J.; Rodriguez-Castellon, E. *Eur. J. Inorg. Chem.* **2006**, 1758.
(25) Liang, F.; Dai, Y. N.; Yi, H. H.; Xiong, X.; Liang, R. *Prog. Chem.* **2008**, *20*, 1606.
(26) Ait-Salah, A.; Dodd, J.; mauger, A.; yazami, R.; Gendron, F.; Julien, C. M. *Z. Anorg. Allg. Chem.* **2006**, 632.
(27) Jain, G.; M, B.; Xu, J. J. *Chem. Mater.* **2006**, *18*, 423.
(28) Kanzaki, S.; Inada, T.; Matsumura, T.; Sonoyama, N.; Yamada, A.; Takano, M.; Kanno, R. *J. Power Sources* **2005**, *146*, 323.
(29) Komba, S.; Suzuki, K.; Kumagai, N. *Electrochemistry* **2002**, *70*, 506.
(30) Kim, J.; Manthiram, A. *J. Electrochem. Soc.* **1999**, *1464*371.
(31) Morales, J.; Santos-Pena, J.; Trocoli, R.; Franger, S.; Rodriguez-Castellon, E. *Electrochim. Acta* **2008**, *53*, 6366.
(32) Larcher, D.; Masquelier, C.; Bonnin, D.; Chabre, Y.; Masson, V.; Leriche, J.-B.; Tarascon, J.-M. *J. Electrochem. Soc.* **2003**, *150*, A133.
(33) Larcher, D.; Bonnin, D.; Cortes, R.; Rivals, I.; Personnaz, L.; Tarascon, J.-M. *J. Electrochem. Soc.* **2003**, *150*, A1643.
(34) Kwon, C. W.; Poquet, A.; Mornet, S.; Campet, G.; Portier, J.; Choy, J. H. *Electrochem. Commun.* **2002**, 197.
(35) Campet, G.; Wen, S. J.; Han, S. D.; Shastry, M.; Portier, J.; Guizard, C.; Cot, L.; Xu, Y. J.; Salardenne, J. *Mater. Sci. Eng., B* **1993**, *18*, 201.
(36) Kwon, C. W.; Quintin, M.; Mornet, S.; Barbieri, C.; Devos, O.; Campet, G.; Delville, M. H. *J. Electrochem. Soc.* **2004**, *151*, A1445.
(37) Poizot, P.; Laruelle, S.; Grugeon, S.; Dupont, L.; Tarascon, J.-M. *Nature* **2000**, *407*, 496.
(38) Goloverda, G.; Jackson, B.; Kidd, C.; Kolesnichenko, V. *J. Mag. Mag. Mater.* **2009**, *321*, 1372.
(39) Ahniyaz, A.; Seisenbaeva, G. A.; Haggstrom, L.; Kamali, S.; Kessler, V. G.; Nordblad, P.; Johansson, C.; Bergstrom, L. *J. Mag. Mag. Mater.* **2008**, 781.
(40) Caruntu, D.; Caruntu, G.; Chen, Y.; O'Connor, C. J.; Goloverda, G.; Kolesnichenko, V. *Chem. Mater.* **2004**, *16*, 5527.
(41) Goya, G. F.; Veith, M.; Rapalavicuite, R.; Shen, H.; Mathur, S. *App. Phys. A: Mater. Sci. Proc.* **2005**, *80*, 1523.
(42) Ismail, A. A. *Appl. Catal. B-Env.* **2005**, *58*, 115.
(43) Veith, M.; Haas, M.; Huch, V. *Chem. Mater.* **2005**, *17*, 95.
(44) Savii, C.; Popovici, M.; enache, C.; Subrt, J.; Niznansky, D.; Bakardzieva, S.; Caiser, C.; Hrianca, I. *Solid State Ionics* **2002**, *151*, 219.
(45) Camargo, P. H. C.; Nunes, G. G.; de Sa, E. L.; Tremiliosi, G.; Evans, D. J.; Zarbin, A. J. G.; Soares, J. F. *J. Brazilian Chem. Soc.* **2008**, *19*, 1501.
(46) Ni, C.; Power, P. P. *Chem. Commun.* **2009**, 5543.
(47) Brandts, J. A. M.; Janssen, M. D.; Hogerheide, M. P.; Boersma, J.; Spek, A. L.; van Koten, G. *Inorg. Chim. Acta* **1999**, 326.
(48) O'Keefe, B. J.; Breyfogle, L. E.; Hillmyer, M. A.; Tolman, W. B. *J. Am. Chem. Soc.* **2002**, *124*, 4384.
(49) Boyle, T. J.; Hernandez-Sanchez, B. A.; Baros, C. M.; Rodriguez, M. A.; Brewer, L. N. *Chem. Mater.* **2007**, *19*, 2016.
(50) Boyle, T. J.; Bunge, S. D.; Alam, T. M.; Holland, G. P.; Headley, T. J.; Avilucea, G. *Inorg. Chem.* **2005**, *44*, 1309.
(51) Boyle, T. J.; Bunge, S. D.; Andrews, N. L.; Matzen, L. E.; Sieg, K.; Rodriguez, M. A.; Headley, T. J. *Chem. Mater.* **2004**, *16*, 3279.
(52) Bunge, S. D.; Boyle, T. J.; Headley, T. J. *Nano Lett.* **2003**, *3*, 901.
(53) Boyle, T. J.; Pratt, H. D.; Hernandez-Sanchez, B. A.; Lambert, T. N.; Headley, T. J. *J. Mater. Sci.* **2007**, *42*, 2792.
(54) Boyle, T. J.; Tribby, L. J.; Ottley, L. A. M.; San, S. M. *Eur. J. Inorg. Chem.* **2009**, *36*, 5550.
(55) Boyle, T. J.; Ottley, L. A. M. *Chem. Rev.* **2008**, *108*, 1896.
(56) Gerung, H.; Boyle, T. J.; Tribby, L. J.; Bunge, S. D.; Brinker, C. J.; Han, S. M. *J. Am. Chem. Soc.* **2006**, *128*, 5244.
(57) Boyle, T. J.; Pedrotty, D. M.; Alam, T. M.; Vick, S. C.; Rodriguez, M. A. *Inorg. Chem.* **2000**, *39*, 5133.
(58) Boyle, T. J.; Andrews, N. L.; Rodriguez, M. A.; Campana, C.; Yiu, T. *Inorg. Chem.* **2003**, *42*, 5357.
(59) Boyle, T. J.; Ottley, L. A. M.; Alam, T. M.; Rodriguez, M. A.; Yang, P.; McIntyre, S. K. *Polyhedron* **2010**, *29*, 1784.
(60) Rodriguez, M. A.; Boyle, T. J.; Yang, P.; Harris, D. L. *Powder Diffraction* **2008**, *23*, 121.
(61) Boyle, T. J.; Ottley, L. A. M.; Rodriguez, M. A.; Sewell, R. M.; Alam, T. M.; McIntyre, S. K. *Inorg. Chem.* **2008**, *47*, 10708.
(62) Bradley, D. C.; Mehrotra, R. C.; Rothwell, I. P.; Singh, A. *Alkoxo and Aryloxo Derivatives of Metals*; Academic Press: San Diego, 2001.
(63) Boyle, T. J.; Ottley, L. A. M.; Brewer, L. N.; Sigman, J.; Clem, P. G.; Richardson, J. J. *Eur. J. Inorg. Chem.* **2007**, 3805.
(64) Boyle, T. J.; Ward, T. L.; De'Angeli, S. M.; Xu, H. F.; Hammetter, W. F. *Chem. Mater.* **2003**, *15*, 765.
(65) Boyle, T. J.; Rodriguez, M. A.; Ingersoll, D.; Headley, T. J.; Bunge, S. D.; Pedrotty, D. M.; De'Angeli, S. M.; Vick, S. C.; Fan, H. Y. *Chem. Mater.* **2003**, *15*, 3903.
(66) Boyle, T. J.; Zechmann, C. A.; Alam, T. M.; Rodriguez, M. A.; Hijar, C. A.; Scott, B. L. *Inorg. Chem.* **2002**, *41*, 946.
(67) Boyle, T. J.; Tafoya, C. J.; Scott, B. L.; Ziller, J. W. *J. Coord. Chem.* **2000**, *51*, 361.
(68) Addison, A. W.; Rao, T. N. *J. Chem. Soc., Dalton Trans.* **1984**, 1349.
(69) Boyle, T. J.; Bunge, S. D.; Clem, P. G.; Richardson, J.; Dawley, J. T.; Ottley, L. A. M.; Rodriguez, M. A.; Tuttle, B. A.; Avilucea, G. R.; Tissot, R. G. *Inorg. Chem.* **2005**, *44*, 1588.
(70) Bunge, S. D.; Boyle, T. J.; Pratt, H. D.; Alam, T. M.; Rodriguez, M. A. *Inorg. Chem.* **2004**, *43*, 6035.
(71) Hermes, A. R.; Girolami, G. S. *Organometallics* **1988**, *7*, 394.
(72) Atkins, P. *Physical Chemistry*, 6th ed.; W. H. Freeman and Co.: New York, 1997.